Dalton Transactions

ROYAL SOCIETY OF CHEMISTRY

PAPER

Cite this: *Dalton Trans.*, 2022, **51**, 17700

Synthesis and evaluation of photocatalytic and photoluminescent properties of Zn^{2+}-doped Bi_2WO_6†

L. X. Lovisa,*[a] T. B. O. Nunes,[b] R. R. Y. O. V. Wilson,[b] E. Longo,[c] M. Daldind,[d] M. R. D. Bomio[b] and F. V. Motta[b]

Received 30th September 2022,
Accepted 2nd November 2022

DOI: 10.1039/d2dt03175b

rsc.li/dalton

This study consists of the synthesis of zinc-doped Bi_2WO_6 obtained by the sonochemical method. The XRD results indicated that the samples showed an orthorhombic phase with the $P2_1ab$ space group without the presence of secondary phases, demonstrating success in the doping process. The results of the photocatalytic tests under the photodegradation of methylene blue showed better performance for the pure sample with 80% degradation during 2 hours of exposure to radiation. The high rate of photogenerated charges accompanied by the low recombination rate of the pairs and e^-/h^+ were responsible for forming hydroxyl radicals, the predominant oxidative agent of the mechanism. The increase in Zn^{2+} concentration in the Bi_2WO_6 matrix promoted inhibition of the photocatalytic properties by the appearance of oxygen vacancies that acted as a charge recombination center. In contrast, photoluminescence was improved by doping with Zn^{2+}. The Bi_2WO_6:8% Zn^{2+} sample showed the highest PL intensity. The characteristics of the emitted colors are modulated from the emission spectra and are quantified in terms of the photometric parameters: chromaticity coordinates (*x*, *y*), color reproduction index (CRI), luminous radiation efficiency (LER), and purity of color (%) of samples. The adjustment in the colors is promoted as a function of the increase in the Zn^{2+} concentration observing the transition from: yellow → orange → green. PL is favored by the effect of the dopant (Zn^{2+}) in the matrix, which allows Bi_2WO_6:Zn^{2+} to be considered a promising candidate for applications in optical devices. In addition, Bi_2WO_6 constitutes a high performance photocatalyst for the degradation of methylene blue.

1. Introduction

The semiconductor-based class of photocatalysts has advanced in many applications. This potentiality is related to the photogenerated charge carriers that participate in the energy transfer in the different optical processes. Inserted in these photocatalysts, bismuth tungstate (Bi_2WO_6) has great potential for application in the degradation of organic pollutants. Its excellent performance is related to the low value of the gap energy, its chemical stability.[1] Yan *et al.*[2] attributes the layered organization of Bi_2WO_6 to the effective separation of the photogenerated loads, promoting a high photocatalytic yield.

Different materials are used in applications of photocatalytic activities, the most renowned is TiO_2 due to its band structure configuration and ability to absorb in the ultraviolet region. However, one of the shortcomings of this material is its high rate of recombination of photogenerated loads, which compromises its response in the degradation of pollutants. A new class of bismuth-based materials ($BiVO_4$, $BiOIO_3$, Bi_2MoO_6, Bi_2WO_6) emerges with favorable physicochemical properties for applications in the field of photocatalysis, as investigated in the works.[3–6] Bi_2WO_6 has an orthorhombic crystal structure, belongs to the Aurivillus family, and presents the general formula of $(Bi_2O_2)^{2+}$ $(A_{m-1}B_mO_{3m+1})^{2-}$. Bi_2WO_6 acts as a heterogeneous photocatalyst by generating electron–hole pairs, which are responsible for originating oxidative species participating in redox reactions on the photocatalyst surface when activated by electromagnetic excitation. The result of this process is the decomposition of a variety of organic pollutants under visible light.[7,8]

Bi_2WO_6 has been used in environmental, energetic, biological areas, involving effluent filtration, water separation, CO_2 reduction, water treatment, air purification, inactivation of bacteria, selective organic synthesis, among others. These

[a]*Institute of Physics and Chemistry, Federal University of Itajuba (UNIFEI), Itajubá, MG, 37500-903, Brazil. E-mail: lauraengmat@hotmail.com*
[b]*LSQM – Laboratory of Chemical Synthesis of Materials – Department of Materials Engineering, Federal University of Rio Grande do Norte, P.O. Box 1524, Natal, RN 59078-900, Brazil*
[c]*CDMF-LIEC, UFSCar, P.O. Box 676, São Carlos, SP 13565-905, Brazil*
[d]*Departamento de Física, Universidade Federal de São Carlos, São Carlos, São Paulo, 13565-905, Brazil*
† Electronic supplementary information (ESI) available. See DOI: https://doi.org/10.1039/d2dt03175b

materials are widely used in the degradation of organic pollutants in wastewater as a way to achieve sustainable mitigation. Bismuth tungstate has been obtained by different routes such as the molten salt route, hydrothermal, solvothermal, sonochemical, sol–gel, and co-precipitation.[3,9–13] The sonochemical method for the synthesis of Bi_2WO_6 nanoparticles has the advantages of simplicity and speed in the process, low energy consumption, and for being a clean method, which ensures the production of materials in a more ecologically sustainable way.[14]

In this work, the photocatalytic and photoluminescent properties of Bi_2WO_6 nanoparticles was studied as function of the Zn^{2+} doping process in Bi_2WO_6:*x*% Zn^{2+} at 1%, 2%, 4% and 8% in mol.

2. Experimental details

2.1 Materials

The reagents used for the synthesis of Bi_2WO_6 and Bi_2WO_6:Zn^{2+} particles were: Bismuth Nitrate III Pentahydrate ($Bi(NO_3)_3{\cdot}5H_2O$), Zinc Acetate Dihydrate ($Zn(OOCCH_3)_2{\cdot}2H_2O$) and Zinc Dihydrate ($Na_2WO_4{\cdot}2H_2O$).

2.2 Preparation of Bi_2WO_6 and Bi_2WO_6:Zn^{2+} particles

Fig. 1 represents the sequence of the experimental procedures adopted to obtain the Bi_2WO_6 and Bi_2WO_6:Zn^{2+} particles. First, two precursor solutions were prepared to obtain the Bi_2WO_6:Zn^{2+} particles: one of tungsten (solution **A**) dissolved in 20 ml of distilled water and the other of bismuth (solution **B**) dissolved in 40 ml of NHO_3 at a concentration of 1 M. The solutions were kept under magnetic stirring and at a temperature of 50 °C for 10 minutes. Solution **A** was dripped into solution **B**. After homogenization of the solution, NH_4OH was added to the solution to stabilize the pH at 7. The solution was stirred for another 30 minutes. The solution was subsequently transferred to an Ultronique EcoSonics QR 550 W ultrasonic processor with a power of 550 W and an ultrasonic frequency of 20 kHz, passing through the synthesis process for 15 minutes. The samples were centrifuged three times in distilled water and then kept in an oven at a temperature of 100 °C for 24 h. Finally, the particles were calcined at a temperature of 800 °C for 2 hours with a heating rate of 10 °C per minute. The procedure for samples doped with Zn^{2+} was similar to that described above. The dopant was stoichiometrically added to the solution at concentrations of 1, 2, 4 and 8% in mol of Zn^{2+}.

2.3 Characterization

The particles were structurally characterized by X-ray diffraction using a Shimadzu 7000 diffractometer. The usage conditions of the diffractometer at the time of analysis were: scanning range from 10 to 80°, angular pitch of 0.020°, scanning speed 1° degrees per minute with Cu Kα radiation (λ = 1.54 Å) of 40 kV and 30 mA. Raman spectroscopy was performed by a Raman HORIBA LabRam HR evolution spectrometer. Diffuse reflectance spectra were obtained using a Shimadzu UV-2600 spectrometer in the region of 200–800 nm programmed for the diffuse reflectance mode. Measurements were performed at room temperature with samples in powder form. The absorption coefficient in the diffuse reflectance spectroscopy spectra in the UV-visible region was expressed by the $F(R)$ function of Kubelka–Munk (1931), $F(R)$, and the band gap energy was estimated based on the theoretical considerations. The absorption coefficient α (λ) of a thin film can be calculated by the following eqn (1), where t is the sample thickness and A is the absorbance:

$$\alpha(\lambda) = 2.303\left(\frac{A}{t}\right) \quad (1)$$

The absorption coefficient near the edge of the absorption band is a function of frequency (eqn (1)), in which: $h\nu$ is the

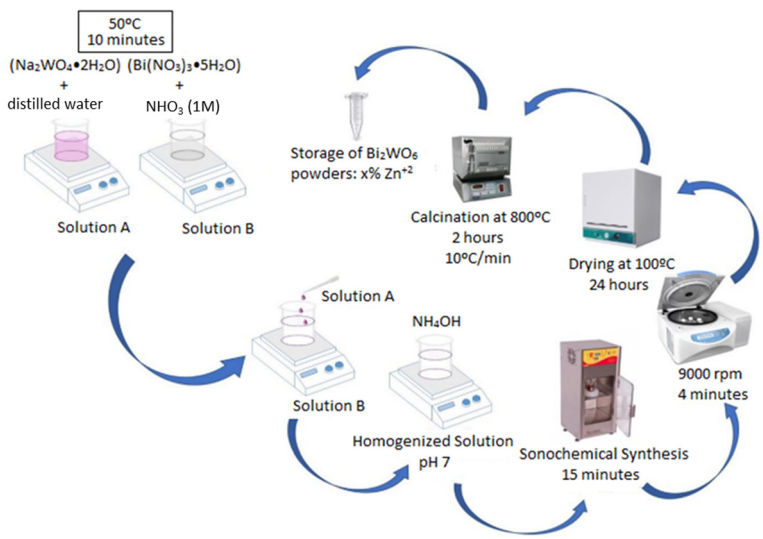

Fig. 1 Sequence of the experimental procedures adopted to obtain the Bi2WO_6 and Bi_2WO_6:Zn^{2+} particles.

photon energy, α is the absorption coefficient, n is a constant that can assume different values for different transitions following well-defined selection rules. So, for allowed direct transitions n = 1/2, for forbidden direct transitions n = 3/2, for allowed indirect transitions n = 2, and for forbidden indirect transitions n = 3. The graphs plotted between ($\alpha h\nu$) on the ordinate axis *vs.* ($h\nu$) the abscissa axis. The straight line extrapolation gives the gap energy value. It is possible to estimate the gap energy value and to have indications about the type of band gap transition through optical absorption measurements.

$$\alpha h\nu = (h\nu - E_g)^n \quad (2)$$

The morphological characteristics of Bi_2WO_6:x% Zn^{2+} were analyzed using a Carl Zeiss Supra 35 VP field emission scanning electron microscope (SEM-FEG).

2.3.1 Photocatalytic activities. The photocatalytic properties of Bi_2WO_6:x% Zn^{2+} were investigated regarding its potential application as a catalytic agent in the degradation of methylene blue dyes. The samples were transported to a photoreactor, kept under stirring with controlled temperature (25 °C) and illuminated by five UV lamps (TUV Philips, 15 W, model G-15T8, with maximum intensity of 254 nm = 4.9 eV). The samples were initially kept under agitation for 20 minutes with the lights off to disregard possible adsorption events. Then, with the lamps on, aliquots of all samples were taken at 20 minute intervals. The variations in the maximum absorption band of the methylene blue dyes (650 nm) were monitored by a Shimadzu UV-2600 photospectrometer within the wavelength range of 400–800 nm.

3. Results

3.1 X-ray diffraction

The Bi_2WO_6 and Bi_2WO_6:Zn^{2+} samples were analyzed by the X-Ray Diffraction technique (XRD) as shown in Fig. 2. Through the analysis, it was possible to observe the microstructural changes of the material as a function of the Zn^{2+} concentration in the Bi_2WO_6 matrix. The diffraction planes identified in the diffractograms are associated with the orthorhombic phase (space group $P2_1ab$) according to the crystallographic reference card.[3] The proportion in mass (mol%) between the reagents was maintained according to stoichiometric calculations, observing the absence of secondary phases. The Zn^{2+} cations introduced into the Bi_2WO_6 matrix partially replaced the Bi^{3+} cation sites without major microstructural distortions. It is observed that the doping process occurs successfully. The structure of Bi_2WO_6 consists of alternating layers of $(Bi_2O_2)_n^{2+}$ and $(WO_2)_n^{2-}$ with shared oxygen atoms connecting these layers. Another way to represent the structure is from the intercalary between the clusters $[(WO_6)^x/(BiO_6)^x]$.[15] The process of replacing $Bi^{3+} \rightarrow Zn^{2+}$ cations cause excess positive charges in the structure. Charge compensation occurs with the formation of oxygen vacancy $V_O^{\cdot\cdot}$, from doping: $[(BiO_6)] + Zn_{Bi}{}^{2+} \rightarrow [(ZnO_6)\cdot V_O^{\cdot\cdot}]$.

The main plane (131) was shifted to a region with a greater angle due to the increase in the concentration of Zn^{2+}. This behavior has been identified by several authors[16,17] and its cause is fundamentally the difference in ionic radii between the host ions and the dopant ions. It is possible to verify a substantial difference between the ionic radii of Bi^{3+} (1.03 Å) and Zn^{2+} (0.70 Å),[18] which justifies distortions generated in the structure of Bi_2WO_6. Wang *et al.*[16] verified similar behavior in the diffraction peak shifts of Bi_2WO_6 doped with Er^{3+}, as well as a reduction in the parameters and lattice spacing due to the dopant effect. Kumar *et al.*[17] observed a displacement in the opposite direction for the smaller angle region, since the dopant Sn^{2+} (1.22 Å) has an ionic radius greater than the Bi^{3+}.

Fig. S1 of ESI† illustrates the Rietveld refinement graph of the obtained Bi_2WO_6 and Bi_2WO_6:x% Zn^{2+} samples. The Bi_2WO_6 (and Bi_2WO_6:x% Zn^{2+}) structure parameters, unit cell volume, bond length and bond angles were obtained and calculated by the Rietveld refinement method using the GSAS (General Structure Analysis System) program with EXPGUI graphical interface.[19] The indication that part of the Bi^{3+} sites were replaced by Zn^{2+} is evidenced in the occupancy data (Occ.) recorded in Table S1 of the ESI.† This information is confirmed by the unit cells modeled using the visualization program for electronic and structural analysis (VESTA)[20] in Fig. S2 of the ESI.† The data obtained with the structural

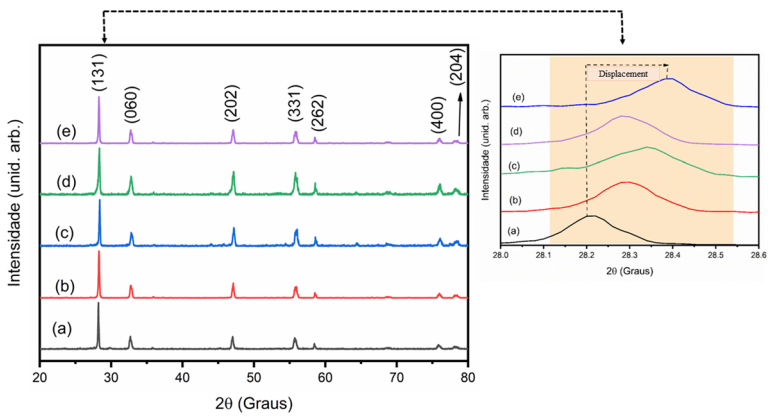

Fig. 2 Diffractograms of Bi_2WO_6 and Bi_2WO_6:x% Zn^{2+} (x = 0, 1, 2, 4 and 8) samples from "a"–"e", respectively.

Table 1 Lattice parameters, crystallite size and quality coefficients of the Rietveld refinement for Bi_2WO_6 and Bi_2WO_6:*x* Zn^{2+} (*x* = 1, 2, 4, 8 mol%) samples

Sample	Bi_2WO_6	Bi_2WO_6:1% Zn^{2+}	Bi_2WO_6:2% Zn^{2+}	Bi_2WO_6:4% Zn^{2+}	Bi_2WO_6:8% Zn^{2+}
System	Orthorhombic	Orthorhombic	Orthorhombic	Orthorhombic	Orthorhombic
Space group	*Pca*21	*Pca*21	*Pca*21	*Pca*21	*Pca*21
a (Å)	5.438	5.439	5.449	5.448	5.438
b (Å)	16.431	16.432	16.428	16.425	16.432
c (Å)	5.460	5.461	5.456	5.455	5.461
V (Å^3)	487.86	488.06	488.40	488.13	487.97
***D* (nm)**	**66.7**	**65.81**	**63.20**	**59.15**	**54.18**
ε ($\times 10^{-4}$)	**3.14**	**3.18**	**3.36**	**3.85**	**3.90**
X^2	2.18	1.31	2.27	2.20	1.21
R_p (%)	16.95	14.25	17.48	17.05	15.84
R_{bragg} (%)	12.03	9.13	13.47	12.43	10.85

refinement of the Bi_2WO_6 and Bi_2WO_6:Zn^{2+} samples are recorded in Table 1. The refinement quality coefficients (R_p, R_f^2, X^2) are within the acceptable limits for the study. It is verified in Fig. 2 a gradual increase in the full-width at maximum (FWHM) of the plane (131) for the doped samples when compared to the Bi_2WO_6 sample. The crystallite size was calculated using the Scherrer equation considering the crystallographic planes (131), (060), (202), (331), (262), (400), (204) located respectively at: 28.7°, 32.7°, 47°, 55.7°, 58.5°, 78.5°, 78°. A small reduction in crystallite size is observed as a function of increasing Zn^{2+} concentration.[21] It is reasonable to consider that the presence of Zn^{2+} modifies the nucleation rate of crystallites, reducing crystal growth, so it is possible to obtain smaller crystallites for the doped samples. The microdeformations are increased in the doped samples due to the greater contribution of the boundary areas between the crystallites, considering in these areas the presence of higher energy (tensions, defects).

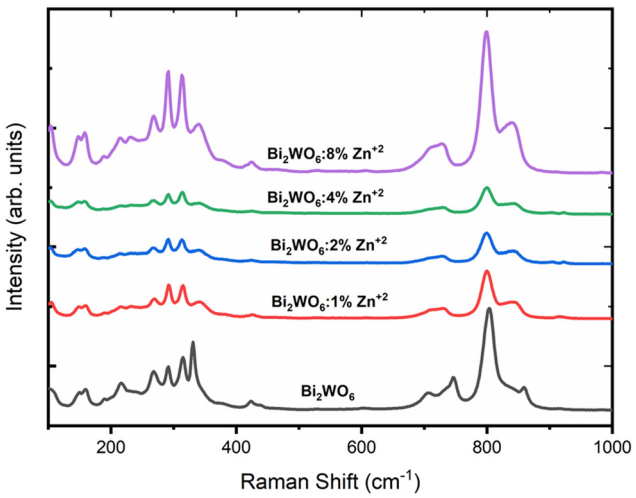

Fig. 3 Raman spectrum of Bi_2WO_6:*x*% Zn^{2+} (*x* = 0, 1, 2, 4 and 8) samples.

3.2 Raman spectroscopy

Raman spectroscopy is a very important technique in the structural and chemical analysis of materials.[22] Analyzes of pure and doped Bi_2WO_6 samples were performed in the range from 100 to 1000 cm^{-1}, as can be seen in Fig. 3. The main Raman band for Bi_2WO_6 is found at 803 cm^{-1}, related to asymmetric stretching between the oxygen and tungstate atoms. The bands located between 250 and 300 cm^{-1} are associated with bending in the chemical bonds between the bismuth and oxygen atoms in the $[Bi_2O_2]^{2+}$ clusters. The band at 314 cm^{-1} is attributed to the synchronous displacement of Bi^{3+} and WO_6^{6-} anions and the band at 155 cm^{-1} is related to the external mode of vibration of WO_6. It is verified that there were no major changes in the positioning of the bands with the Zn^{2+} ions doping process in the Bi_2WO_6 matrix, this behavior was recorded by Wang *et al.*[23] The Fig. 3 shows the reduction in Raman intensity with increasing Zn^{2+} level for samples doped with 1, 2 and 4%. Such a reduction in the Raman bands may be related to the decrease in crystallite sizes, which may promote an increase in the density of surface defects according to the data presented in Table 1 for the parameters: *D* (crystallite size) and ε (microstrain). This behavior is similar to that found by Keerthana *et al.*[24] who performed the Ni doping of Bi_2WO_6. There is an amplification of all Raman peaks for the sample doped with 8% Zn^{2+}, which may indicate the presence of oxygen vacancy defects as observed by Li *et al.*[25,26]

3.3 Field emission scanning electron microscopy (SEM-FEG)

It was possible to observe different types of particle morphologies from the analysis of SEM-FEG images performed on the Bi_2WO_6 and Bi_2WO_6:Zn^{2+} samples in Fig. 4. The Bi_2WO_6 sample has spherical shaped particles. The order of magnitude of the size of these particles is between nanometers and a few micrometers. The heat treatment performed on the samples favored the coalescence of the particles, it is observed that the particles present a certain level of agglomeration. However, it is possible to clearly identify the interface line between the particles, which means that the individual characteristics of the particles were maintained. In the sample Bi_2WO_6:1% Zn^{2+}, polyhedral particles with a very regular face plane were identified, as shown in inset. The presence of pores on the surfaces of the crystals is revealed, as well as, in the interception of the crystals as represented in the sample Bi_2WO_6:4% Zn^{2+}. The

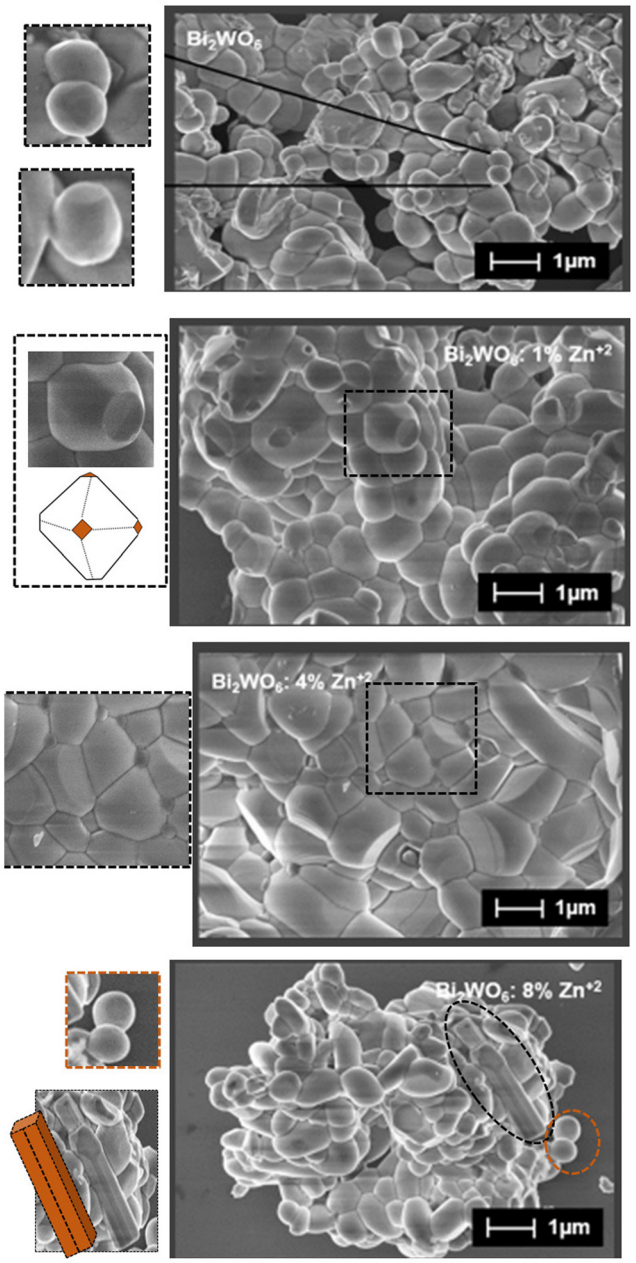

Fig. 4 Micrographs obtained by SEM-FEG of Bi_2WO_6 and Bi_2WO_6:*x*% Zn^{2+} (*x* = 1%, 4% and 8%) samples, respectively.

sample Bi_2WO_6:8% Zn^{2+} presents particles with varied morphologies. It is evident the presence of irregular particles, as well as particles with specific characteristics, such as microrod (preferential growth) and nanospheres. Similar aspects were found with other works reported in the literature.[16,17] F. J. Zhang *et al.*[27] relates morphological characteristics of Bi_2WO_6 to the conditions used in the sonochemical method. Fig. S3† represents EDS analysis in Bi_2WO_6 and Bi_2WO_6:8% Zn^{2+} samples. Quantitative chemical analysis expresses an estimate of the percentage of each element that makes up the sample. Considering that there is a margin of inaccuracy due to the capture limitation of the equipment.

3.4 Spectroscopy in the UV-visible (UV-vis) region

The optical properties of Bi_2WO_6 and Bi_2WO_6:*x*% Zn^{2+} samples were investigated by UV-vis diffuse reflectance spectra. These measurements are important for the photocatalytic performance of the material studied. As shown in Fig. 5, Bi_2WO_6 has an absorption threshold of approximately 400 nm. After doping with Zn^{2+}, the absorption of visible light appears to increase. It is observed a deviation from the absorption edge to the red region, a similar observation was made by Wang *et al.*[28] Bi_2WO_6:2% Zn^{2+} and Bi_2WO_6:4% Zn^{2+} samples showed the highest red shift at the absorption edge compared to the other samples. The absorption is a result of the hybridization of O 2p and Bi 6s orbitals forming the valence band (VB), while the conduction band (CB) has major contributions from the W 5d orbitals.[26,29]

The gap energy of Bi_2WO_6 and Bi_2WO_6:*x*% Zn^{2+} was estimated from the Kubelka–Munk transformation. As shown in the literature, Bi_2WO_6 is a direct optical transition semiconductor.[29] Fig. 6 represents the gap energies that are estimated at: 2.93, 2.87, 2.95, 2.82 and 2.94 eV for the respective samples: Bi_2WO_6, Bi_2WO_6:1% Zn^{2+}, Bi_2WO_6:2% Zn^{2+}, Bi_2WO_6:4% Zn^{2+} and Bi_2WO_6:8% Zn^{2+}. The E_{gap} values found in this work are in agreement with other works reported in the literature.[30,31] Small variations in E_{gap} values are observed as a function of Zn^{2+} concentration. The estimated E_{gap} values represent an average of each face that constitutes the Bi_2WO_6 particles. The replacement of the Bi^{3+} ion by the Zn^{2+} ion causes changes in the structure of the energy bands through the appearance of intermediate energy levels in the band gap. This new arrangement of the band structures is a way to neutralize the existing loads due to the $Bi^{3+} \rightarrow Zn^{2+}$ substitution, generating defects in the material's structure.

3.5 Photocatalytic activity tests

The samples were initially kept in the degradation chamber with the lamps off for 20 minutes to obtain the adsorption–de-

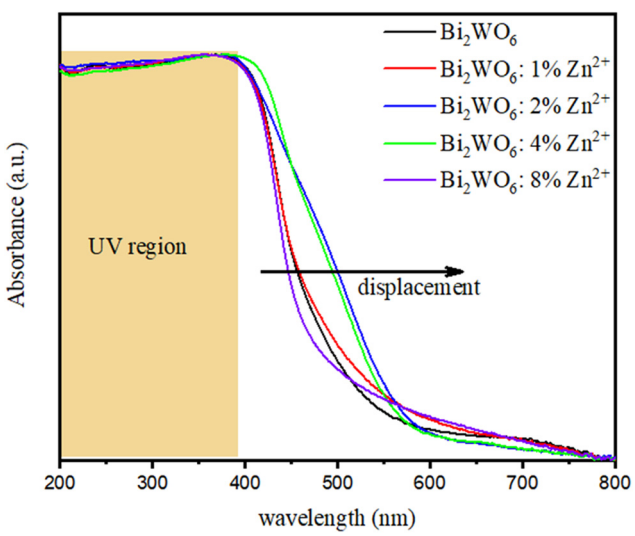

Fig. 5 Diffuse UV-vis reflectance spectra of Bi_2WO_6 and Bi_2WO_6:*x*% Zn^{2+}.

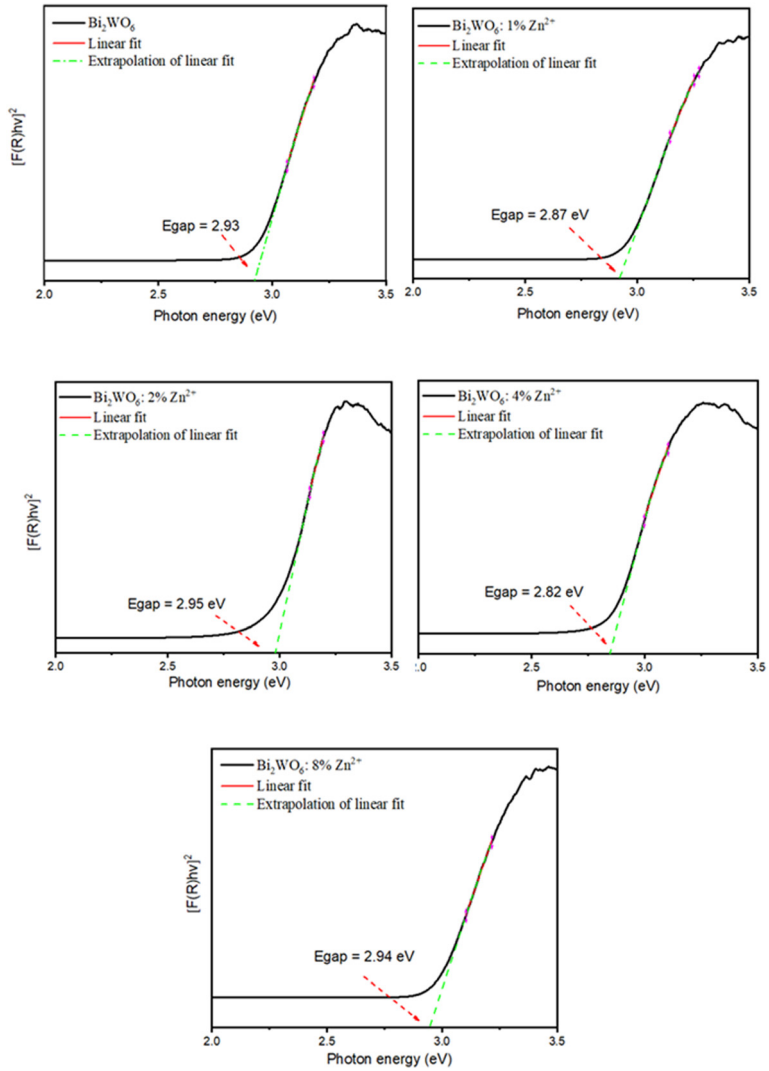

Fig. 6 Determination of the gap energy of Bi_2WO_6 and Bi_2WO_6:*x*% Zn^{2+}.

sorption equilibrium on the catalyst surface. This was in order to ensure that any and all dye degradation observed was due to the action of the catalyst when starting the reaction. Based on the behavior of the absorbance curves, a calibration curve was constructed to determine the methylene blue concentration (C/C_0). From this curve, it was possible to calculate how much (%) each sample was degraded. Fig. 7 shows the methylene blue concentration as a function of irradiation time, corresponding to Bi_2WO_6 and Bi_2WO_6:*x*% Zn^{2+} (x = 1, 2, 4 and 8) Samples. It was observed that Bi_2WO_6 presented better performance in reducing the methylene blue dye concentration when subjected to UV radiation during the photocatalytic tests.

The photocatalytic efficiency presented by Bi_2WO_6 is associated with a higher efficiency of charge separation photogenerated by irradiation ($h\nu$). The generated electrons migrate to the surface of Bi_2WO_6, inducing oxidation and reduction reactions with adsorbed species (H_2O, H^-, O_2, CO_2, organic com-

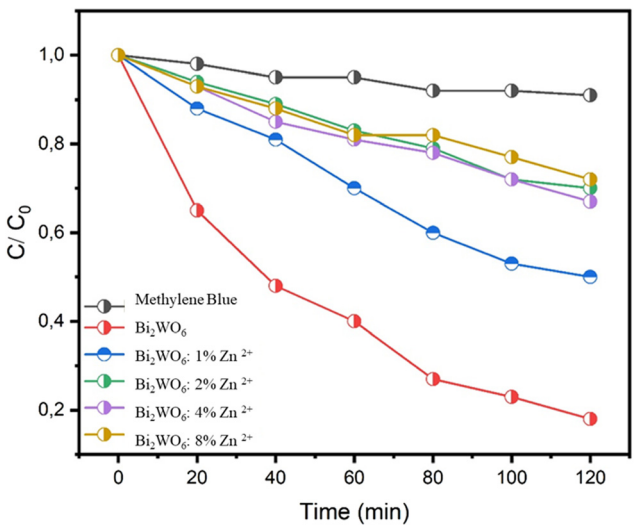

Fig. 7 Variation of methylene blue concentration *versus* time under UV irradiation for Bi_2WO_6 and Bi_2WO_6:*x*% Zn^{2+} (x = 1, 2, 4 and 8) samples.

pounds). The holes generated in[32] the valence band are efficient oxidizing agents. In contrast, conduction band electrons are good reducers. The holes act by oxidizing the water adsorbed on the semiconductor surface, generating hydroxyl radicals, which subsequently oxidize the organic compounds into smaller and less polluting molecules or even completely oxidize them to CO_2 and H_2O. Zhang *et al.*[33] investigated that the photocatalytic performance of Bi_2WO_6 for RhB degradation is closely associated with particle shape, size and structure characteristics. Phu *et al.*[34] reported high photocatalytic activity of Bi_2WO_6 due to its efficient transport of photogenerated charges to active sites on the catalyst surface.

It is observed that the increase in the Zn^{2+} concentration promoted a significant decrease in the photocatalytic activity on the methylene blue dye. However, the substitution of the Bi^{3+} cation for the Zn^{2+} cation causes changes in the structure of the energy bands, as verified in the Spectroscopy analysis in the UV-visible region by the gap energy estimate. The appearance of defects, such as oxygen vacancies $(V_O^{\cdot\cdot})$, can behave as a center of recombination of electron–hole charges in order to negatively affect the photocatalytic performance of Bi_2WO_6. Le *et al.*[35] observed that introducing Fe^{3+} ions into the ZnO structure caused a suppression in the photocatalytic activities as a result of the emergence of new defects that act as charge recombination centers. Similar behavior was registered by the authors Andrade Neto *et al.*[36] and Vanheusden *et al.*[37] in their respective works.

Another possibility that can be evaluated is the influence that Zn^{2+} had on the surface area of Bi_2WO_6 particles. Given the results of the photocatalytic tests, there is probable indication that the surface area was compromised by the introduction of Zn^{2+} into the Bi_2WO_6 structure.

Fig. 8 represents the methylene blue dye degradation percentage for each sample. It is verified that the pure sample presented a higher degradation percentage in relation to the samples doped with Zn^{2+}. Bi_2WO_6 degrades 82% of the MB dye. However, the dye degradation efficiency significantly reduces as the Zn^{2+} concentration increases, reaching lower values of: 50, 30, 33 and 28% for the respective Bi_2WO_6:1% Zn^{2+}, Bi_2WO_6:2% Zn^{2+}, Bi_2WO_6:4% Zn^{2+} and Bi_2WO_6:8% Zn^{2+} samples.

The kinetic constant is an important tool to estimate the catalytic behavior of semiconductor materials. In this work, the photocatalytic kinetic constant was estimated from the linearization of the catalytic data to better analyze the photocatalytic activity represented in Fig. 9. The photocatalytic constants of the pure and doped samples with 1, 2, 4 and 8 mol% Zn^{2+} were 1.67×10^{-2}; 0.60×10^{-2}; 0.31×10^{-2}; 0.35×10^{-2} and 0.30×10^{-2} min^{-1}, respectively. The values obtained in this study illustrate the negative effect of doping, where the catalytic kinetics decreases by 6× when Bi_2WO_6 is doped with zinc. On the other hand, it can be observed that the photocatalytic results are consistent with the photoluminescent analyses, where doping increased the recombination rate of the e^-/h^+ pairs, disfavoring the photocatalytic activity and favoring the photoluminescent activity.

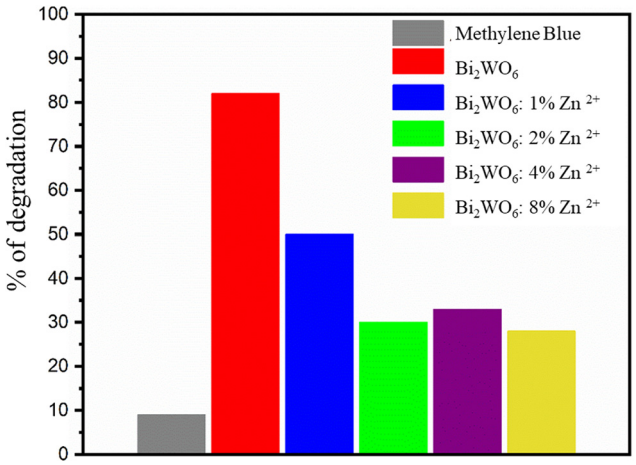

Fig. 8 Graph of the degradation percentage of the methylene blue dye for Bi_2WO_6 and Bi_2WO_6:*x* Zn^{2+} (*x* = 1, 2, 4 and 8 mol%) samples under UV irradiation.

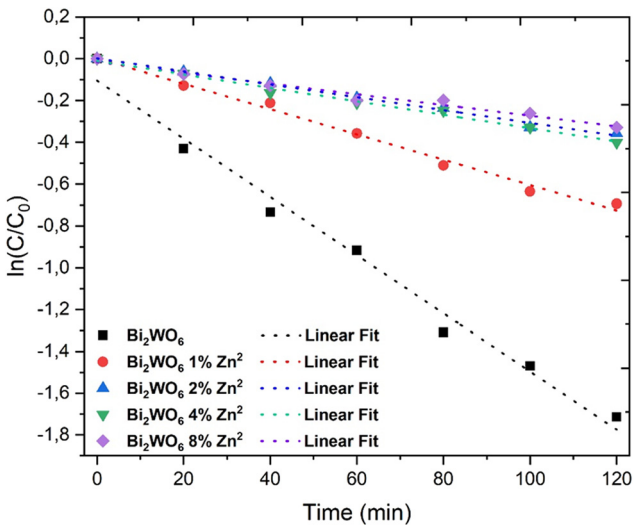

Fig. 9 Photocatalytic constants of the Bi_2WO_6 and Bi_2WO_6:Zn^{2+}.

3.6 Reuse tests

Reuse tests were performed to evaluate the chemical stability of the material. Thus, the sample which presented the best efficiency during the photocatalytic test, namely the pure Bi_2WO_6 sample, was used to do so. At the end of the photocatalytic cycle, the sample was centrifuged, washed and dried for 24 hours in an oven at 90 °C. After drying, the sample was submitted to the photocatalytic reuse process. Two photocatalytic reuses were performed and, according to Fig. 10, it can be seen that the efficiency of Bi_2WO_6 decreased with reuse cycles by 25%. The loss of efficiency may have occurred due to saturation and poisoning of the photocatalyst[17].

The scavenger method was used to evaluate which is the main mechanism that acts in the photocatalytic process in the degradation of the methylene blue dye. For this evaluation, the sample that presented the best photocatalytic efficiency (pure

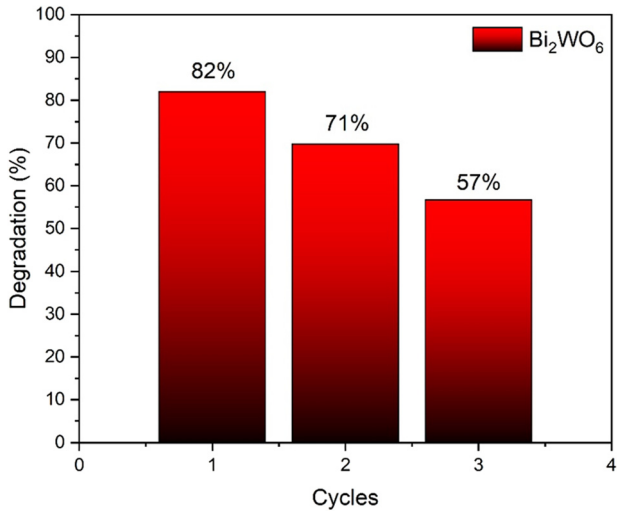

Fig. 10 Photocatalytic and reuse cycles of the Bi_2WO_6 sample.

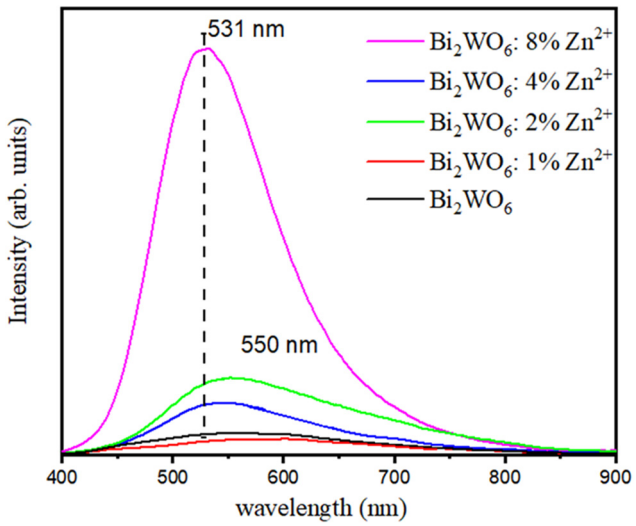

Fig. 12 Bi_2WO_6 and Bi_2WO_6 PL emission spectrum:x% Zn^{2+}.

sample) was used, as well as $AgNO_3$ (AG), EDTA, isopropyl alcohol and ascorbic acid (AA) in order to suppress the action of e^-, h^+, $^{\bullet}OH$ e O^{2-}, respectively.[38,39] From the graph of C/C_0 *versus* time (Fig. 11) it is possible to observe that the presence of EDTA, IPA and AA considerably suppressed the photocatalytic efficiency of the pure sample, with IPA being the greatest inhibitor at the end of the photocatalytic cycle. This means that the hydroxyl radical ($^{\bullet}OH$) is the most active mechanism for the pure sample, being the same responsible for oxidizing the dye molecules.

3.7 Photoluminescence measurements

Fig. 12 shows the photoluminescence emission spectra of Bi_2WO_6:x Zn^{2+} (x = 1, 2, 4 and 8 mol%) samples. Measurements were performed at room temperature at an excitation wavelength (λ_{exc}) of 325 nm. The PL spectra demonstrate a broadband profile. This property is related to an electron relaxation process that includes several energy levels (E_n, $n > 0$) for low energy states (E_0). These excited energy levels are located near to each other. Due to this approximation, there is a mutual cooperation between these electronic transitions within the band gap. Thus, the PL spectral distribution is a function of a multilevel and multiphonic process.[40] The photoluminescence of tungstates is substantially related to configurations presented by the $[WO_4]^{2-}$ clusters in terms of structural distortions that promote changes in the structure of energy bands by the insertion of intermediate levels in the band gap. According to Marques *et al.*,[41] the excitation process occurs by energy absorption in a low energy state [O(2p)] and excitation to higher energy states [W(5d)].

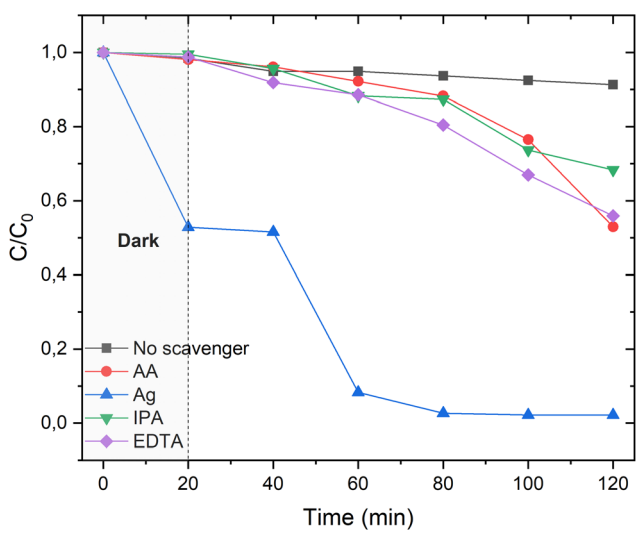

Fig. 11 The scavenger method.

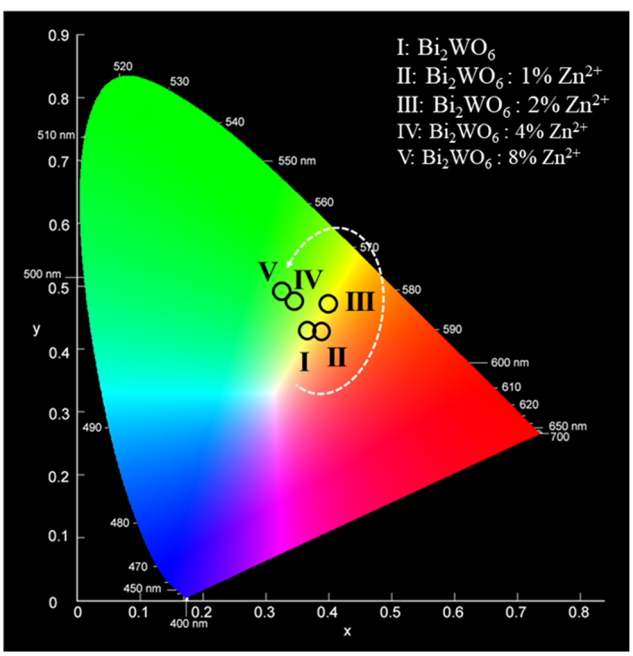

Fig. 13 Representation of the chromaticity coordinates of Bi_2WO_6 and Bi_2WO_6:x% Zn^{2+} in the CIE Diagram.

Table 2 Color properties: chromaticity coordinates (x, y), CRI, LER, CCT and purity of Bi_2WO_6 and Bi_2WO_6:Zn^{2+} samples

Sample	Bi_2WO_6	Bi_2WO_6:1% Zn^{2+}	Bi_2WO_6:2% Zn^{2+}	Bi_2WO_6:4% Zn^{2+}	Bi_2WO_6:8% Zn^{2+}
(X_i, Y_i)	0.37, 0.42	0.39, 0.42	0.40, 0.47	0.34, 0.48	0.33, 0.49
Color	Yellow	Yellow	Orange	Green	Green
CRI (%)	83	87	75	66	58
LER	280	249	300	316	377
CCT (K)	4361	3852	4056	—	—
Purity (%)	40.6	46.2%	63.5%	48.7	49.6

It is observed that the increase in the Zn^{2+} concentration in the Bi_2WO_6 structure promoted a shift in the emission band to the higher energy region. This gradual transition of the emission region between the yellow Bi_2WO_6 sample to the green emission region of the Bi_2WO_6:8% Zn^{2+} sample is quite significant, as shown in the spectra of Fig. 12. Fundamentally, the different types of structural arrangements and changes in energy transfers within $[WO_4]^{2-}$ clusters can promote changes in PL behavior as shown in Fig. 12. Lovisa *et al.*[42] report that according to the types of defects found in the material structure, it is possible to associate the displacements performed in the emission bands. The position of the defects in the bandgap promotes specific recombination centers between the electrons + holes pairs which, therefore, promote different transitions in the different bands within the visible region. Thus, the emissions in the yellow-red region are attributed to the deep defects (structural disorder and oxygen vacancies in the $[WO_4]^{2-}$) region, as well as the emissions in the blue-green region are attributed to the surface defects.

Another aspect observed was the increase in photoluminescence intensity together with the increase in Zn^{2+} concentration. It is reasonable to consider that the presence of Zn^{2+} in the Bi_2WO_6 matrix favored the photoluminescent property due to the increase in the recombination rate of photogenerated charges by the substitution of $Bi^{3+} \rightarrow Zn^{2+}$ ions. This consideration is not evaluated in isolation. Lovisa *et al.*[43] identify these disorders in classes of defects particularly: elongation/shortening of [W–O] bonds, changes in bond angles, emergence of structural defects such as oxygen vacancy. The photoluminescence and photocatalysis properties present an inverse behavior with each other as a function of the increase in the Zn^{2+} concentration in the Bi_2WO_6 matrix. This effect is related to the increase in the rate of charge recombination of electrons + holes, which enhances photoluminescence and, simultaneously, inhibits photocatalysis.

According to the spectral distribution shown in Fig. 13, it was possible to calculate the photometric parameters as well as characterizing and evaluating the quality of the light emitted as a function of the effects produced by the Zn^{2+} concentration. All these parameters are recorded in Table 2. Fig. 13 presents the CIE chromaticity diagram indicating the emission region of each sample and their respective chromaticity coordinates (xc, yc). There is a change in the emission region from the increase in the Zn^{2+} concentration in the Bi_2WO_6 lattice. As indicated in Fig. 13, it is observed that the gradual increase in the concentration of Zn^{2+} in Bi_2WO_6 provides a modulation in the emission color observing the following sequence: yellow → orange → green.

4. Conclusion

In summary, Bi_2WO_6 and Bi_2WO_6:Zn^{2+} particles obtained by the simple sonochemistry method are described. Promising results were presented in photocatalysis and photoluminescence. The experimental results indicate that the photocatalytic performance is associated with the efficiency in separating photogenerated charges. The predominant action of hydroxyl radicals in the oxidizing action of the pollutant was considered in the photocatalysis mechanism. The efficient transport of photogenerated charges to active sites on the catalyst surface may be related to the high photocatalytic activity of Bi_2WO_6. Doping with Zn^{2+} did not effectively favor the photocatalytic property due to the recombination rate of electron–hole charges by trapping the oxygen vacancies ($V_O^{\cdot\cdot}$). The photoluminescent behavior was simultaneously improved with increasing Zn^{2+} concentration. The Bi_2WO_6:8% Zn^{2+} sample presented the maximum PL intensity which was attributed to the structural disorders that exert modifications in the length of the bonds and in the bond angles. The adjustment of the colors emitted by the Bi_2WO_6:Zn^{2+} particles was related to the types of structural defects present in the Bi_2WO_6 matrix evidenced by the shifts of the PL spectra. Other considerations were made regarding the photometric characteristics of the samples.

Conflicts of interest

The authors declare that they have no conflict of interest.

Acknowledgements

The authors wish to thank the financial support of the following Brazilian research funding agencies: the National Council for Scientific and Technological Development (CNPq), the Coordination for the Improvement of Higher Education Personnel (CAPES) and the Graduate Program in Materials Science and Engineering (PPGCEM/UFRN).

References

1 C.-H. Wu, C.-Y. Kuo, J.-T. Wu, M.-J. Hsu and T.-J. Jhang, Photodegradation of CI Reactive Red 2 in the Bi2WO6 system: the determination of surface characteristics and photocatalytic activities of Bi2WO6, Reaction Kinetics, *Mech. Catal.*, 2016, **117**, 391–404.

2 P. Yan, D. Li, X. Ma, J. Xue, Y. Zhang and M. Liu, Hydrothermal synthesis of Bi 2 WO 6 with a new tungsten source and enhanced photocatalytic activity of Bi 2 WO 6 hybridized with C 3 N 4, *Photochem. Photobiol. Sci.*, 2018, **17**, 1084–1090.

3 J. Chen, H. Lei, S. Ji, M. Wu, B. Zhou and X. Dong, Synergistic catalysis of BiOIO3 catalyst for elimination of organic pollutants under simultaneous photo-irradiation and ultrasound-vibration treatment, *J. Colloid Interface Sci.*, 2021, **601**, 704–713.

4 H. Hori, M. Takase, M. Takashima, F. Amano, T. Shibayama and B. Ohtani, Mechanism of formation, structural characteristics and photocatalytic activities of hierarchical-structured bismuth-tungstate particles, *Catal. Today*, 2018, **300**, 99–111.

5 R. Koutavarapu, B. Babu, C. V. Reddy, I. N. Reddy, K. R. Reddy, M. Rao, T. M. Aminabhavi, M. Cho, D. Kim and J. Shim, ZnO nanosheets-decorated Bi2WO6 nanolayers as efficient photocatalysts for the removal of toxic environmental pollutants and photoelectrochemical solar water oxidation, *J. Environ. Manage.*, 2020, **265**, 110504.

6 S. Ye, Y. Xu, L. Huang, W. Lai, L. Deng, Z. Lin, H. Peng, X. Zhou and G. Xie, MWCNT/BiVO4 photocatalyst for inactivation performance and mechanism of Shigella flexneri HL, antibiotic-resistant pathogen, *Chem. Eng. J.*, 2021, **424**, 130415.

7 Q. Li, Z. Guan, D. Wu, X. Zhao, S. Bao, B. Tian and J. Zhang, Z-scheme BiOCl-Au-CdS heterostructure with enhanced sunlight-driven photocatalytic activity in degrading water dyes and antibiotics, *ACS Sustainable Chem. Eng.*, 2017, **5**, 6958–6968.

8 R. Radha, R. V. Kulangara, E. Elaiyappillai, J. Sridevi and S. Balakumar, Modulation in the band dispersion of Bi2WO6 nanocrsytals using the electronegativity of transition elements for enhanced visible light Photocatalysis, *Cryst. Growth Des.*, 2019, **19**, 6224–6238.

9 A. Martínez-de la Cruz and S. O. Alfaro, Synthesis and characterization of γ-Bi2MoO6 prepared by co-precipitation: photoassisted degradation of organic dyes under vis-irradiation, *J. Mol. Catal. A: Chem.*, 2010, **320**, 85–91.

10 T. Chankhanittha, V. Somaudon, T. Photiwat, K. Hemavibool and S. Nanan, Preparation, characterization, and photocatalytic study of solvothermally grown CTAB-capped Bi2WO6 photocatalyst toward photodegradation of Rhodamine B dye, *Opt. Mater.*, 2021, **117**, 111183.

11 R. Song, N. Chen, B. Han, S. Yu, Y. Wang, K. Liu, Z. Tong and H. Zhang, Microwave hydrothermal fabrication of 3D hierarchical Br/Bi2WO6 with enhanced photocatalytic activity for Rhodamine B and tetracycline degradation, *Environ. Sci. Pollut. Res.*, 2021, **28**, 36434–36452.

12 S. Balakumar, N. Mahesh, M. Kamaraj, S. Shyamalagowri, J. Manjunathan, S. Murugesan, J. Aravind and P. Suresh Babu, Outlook on bismuth-based photocatalysts for environmental applications: A specific emphasis on Z-scheme mechanisms, *Chemosphere*, 2022, **203**, 135052.

13 G. Zhang, F. Lü, M. Li, J. Yang, X. Zhang and B. Huang, Synthesis of nanometer Bi_2WO_6 synthesized by sol–gel method and its visible-light photocatalytic activity for degradation of 4BS, *J. Phys. Chem. Solids*, 2010, **71**, 579–582.

14 A. V. Karim and A. Shriwastav, Degradation of amoxicillin with sono, photo, and sonophotocatalytic oxidation under low-frequency ultrasound and visible light, *Environ. Res.*, 2021, **200**, 111515.

15 I. M. Pinatti, F. A. Pires, P. B. Almeida, P. F. Pereira, M. D. Teodoro, E. Guillamón, A. Z. Simões, J. Andrés, E. Longo and I. L. Rosa, Tailoring Bi2MoO6 by Eu3+ incorporation for enhanced photoluminescence emissions, *J. Lumin.*, 2022, **243**, 118675.

16 M. Wang, Z. Qiao, M. Fang, Z. Huang, Y. g. Liu, X. Wu, C. Tang, H. Tang and H. Zhu, Synthesis of Er-doped Bi 2 WO 6 and enhancement in photocatalytic activity induced by visible light, *RSC Adv.*, 2015, **5**, 94887–94894.

17 B. V. Kumar, M. D. Prasad and M. Vithal, Enhanced visible light photocatalytic activity of Sn doped Bi2WO6 nanocrystals, *Mater. Lett.*, 2015, **152**, 200–202.

18 F. Ren, J. Zhang and Y. Wang, Enhanced photocatalytic activities of Bi 2 WO 6 by introducing Zn to replace Bi lattice sites: a first-principles study, *RSC Adv.*, 2015, **5**, 29058–29065.

19 B. H. Toby, EXPGUI, a graphical user interface for GSAS, *J. Appl. Crystallogr.*, 2001, **34**, 210–213.

20 K. Momma and F. Izumi, VESTA 3 for three-dimensional visualization of crystal, volumetric and morphology data, *J. Appl. Crystallogr.*, 2011, **44**, 1272–1276.

21 L. Xiang, L. Chen, C.-H. Mo, L.-M. Zheng, Z.-X. Yu, Y.-W. Li, Q.-Y. Cai, H. Li, W.-D. Yang and D.-M. Zhou, Facile synthesis of Ni-doping Bi2WO6 nano-sheets with enhanced adsorptive and visible-light photocatalytic performances, *J. Mater. Sci.*, 2018, **53**, 7657–7671.

22 D. Titus, E. J. J. Samuel and S. M. Roopan, Nanoparticle characterization techniques, in *Green synthesis, characterization and applications of nanoparticles*, Elsevier, 2019, pp. 303–319.

23 R. Wang, Z. Jiang, L. Xu and C. Liu, Synthesis of Dy(III) doped Bi2WO6 photocatalyst with highly efficient photocatalytic performance under simulated sunlight, *J. Mater. Sci.: Mater. Electron.*, 2021, **32**, 6931–6941.

24 S. Keerthana, B. J. Rani, G. Ravi, R. Yuvakkumar, S. Hong, D. Velauthapillai, B. Saravanakumar, M. Thambidurai and C. Dang, Ni doped Bi2WO6 for electrochemical OER activity, *Int. J. Hydrogen Energy*, 2020, **45**, 18859–18866.

25 C. Li, G. Chen, J. Sun, H. Dong, Y. Wang and C. Lv, Construction of Bi2WO6 homojunction via QDs self-decoration and its improved separation efficiency of charge

carriers and photocatalytic ability, *Appl. Catal., B*, 2014, **160**, 383–389.
26 M. d. J. S. Chaves, G. de Oliveira Lima, M. de Assis, C. d. J. S. Mendonça, I. M. Pinatti, A. F. Gouveia, I. L. V. Rosa, E. Longo, M. A. P. Almeida and T. C. R. dos Santos Franco, Environmental remediation properties of Bi2WO6 hierarchical nanostructure: A joint experimental and theoretical investigation, *J. Solid State Chem.*, 2019, **274**, 270–279.
27 F.-J. Zhang, F.-Z. Xie, J. Liu, W. Zhao and K. Zhang, Rapid sonochemical synthesis of irregular nanolaminar-like Bi2WO6 as efficient visible-light-active photocatalysts, *Ultrason. Sonochem.*, 2013, **20**, 209–215.
28 Q. Wang, Q. Lu, L. Yao, K. Sun, M. Wei and E. Guo, Preparation and characterization of ultrathin Pt/CeO_2/Bi2WO6 nanobelts with enhanced photoelectrochemical properties, *Dyes Pigm.*, 2018, **149**, 612–619.
29 I. M. Pinatti, A. F. Gouveia, C. Doñate-Buendía, G. Mínguez-Vega, J. Andres and E. Longo, Femtosecond-laser-irradiation-induced structural organization and crystallinity of Bi2WO6, *Sci. Rep.*, 2020, **10**, 1–14.
30 X. Liu, Q. Lu, C. Zhu and S. Liu, Enhanced photocatalytic activity of α-Fe 2 O 3/Bi 2 WO 6 heterostructured nanofibers prepared by electrospinning technique, *RSC Adv.*, 2015, **5**, 4077–4082.
31 D. Huang, J. Li, G. Zeng, W. Xue, S. Chen, Z. Li, R. Deng, Y. Yang and M. Cheng, Facile construction of hierarchical flower-like Z-scheme AgBr/Bi2WO6 photocatalysts for effective removal of tetracycline: Degradation pathways and mechanism, *Chem. Eng. J.*, 2019, **375**, 121991.
32 G. Zhu, J. Liang, M. Hojamberdiev, S. A. Bilmes, X. Wei, P. Liu and J. Zhou, Ethylenediamine (EDA)–assisted hydrothermal synthesis of nitrogen-doped Bi2WO6 powders, *Mater. Lett.*, 2014, **122**, 216–219.
33 L. Zhang, W. Wang, L. Zhou and H. Xu, Bi2WO6 nano–and microstructures: shape control and associated visible–light–driven photocatalytic activities, *Small*, 2007, **3**, 1618–1625.
34 N. D. Phu, L. H. Hoang, X.-B. Chen, M.-H. Kong, H.-C. Wen and W. C. Chou, Study of photocatalytic activities of Bi2WO6 nanoparticles synthesized by fast microwave-assisted method, *J. Alloys Compd.*, 2015, **647**, 123–128.
35 T. H. Le, A. T. Bui and T. K. Le, The effect of Fe doping on the suppression of photocatalytic activity of ZnO nanopowder for the application in sunscreens, *Powder Technol.*, 2014, **268**, 173–176.
36 N. A. Neto, K. Matsui, C. Paskocimas, M. Bomio and F. Motta, Study of the photocatalysis and increase of antimicrobial properties of Fe3+ and Pb2+ co-doped ZnO nanoparticles obtained by microwave-assisted hydrothermal method, *Mater. Sci. Semicond. Process.*, 2019, **93**, 123–133.
37 K. Vanheusden, W. Warren, J. Voigt, C. Seager and D. Tallant, Impact of Pb doping on the optical and electronic properties of ZnO powders, *Appl. Phys. Lett.*, 1995, **67**, 1280–1282.
38 S. Balasurya, A. Syed, L. L. Raju, S. Al-Rashed, A. M. Thomas, A. Das and S. S. Khan, Elucidation of photocatalysis, photoluminescence and antibacterial studies of Ag2MoO4 decorated NiMoO4 nano-heterostructure, *Opt. Mater.*, 2021, **113**, 110856.
39 M. K. Hussain and N. Khalid, Surfactant-assisted synthesis of MoO3 nanorods and its application in photocatalytic degradation of different dyes in aqueous environment, *J. Mol. Liq.*, 2022, **346**, 117871.
40 L. Lovisa, A. Santiago, M. Farias, B. Barros, E. Longo, M. S. Li, C. Paskocimas, M. Bomio and F. Motta, White light emission from single-phase Y2MoO6: xPr3+ (x = 1, 2, 3 and 4 mol%) phosphor, *J. Alloys Compd.*, 2018, **769**, 420–429.
41 A. P. de Azevedo Marques, R. Künzel, N. K. Umisedo, R. M. Latini, E. M. Yoshimura and E. Okuno, Tm3+ doped barium molybdate: A potential long-lasting blue phosphor, *J. Alloys Compd.*, 2018, **735**, 707–717.
42 L. Lovisa, D. F. Dos Santos, A. Santiago, M. Siu Li, E. Longo, F. Motta and M. Bomio, Enhanced red emission in Sr (1-x) EuxMo0. 5 W0. 5O4 (x = 0.01, 0.02, 0.04) phosphor and spectroscopic analysis for display applications, *J. Mater. Sci.*, 2022, **57**, 8634–8647.
43 L. Lovisa, Y. Fernandes, L. Garcia, B. Barros, E. Longo, C. Paskocimas, M. Bomio and F. Motta, Tb3+/Pr3+ co-doped ZnMoO4 phosphor with tunable photoluminescence and energy transfer processes, *Opt. Mater.*, 2019, **96**, 109332.

